Novel high temperature proton conducting fuel cells: Production of La$_{0.995}$Sr$_{0.005}$NbO$_{4-\delta}$ electrolyte thin films and compatible cathode architectures

M.-L. Fontaine [a,*], Y. Larring [a], R. Haugsrud [b], T. Norby [b], K. Wiik [c], R. Bredesen [a]

[a] SINTEF Materials and Chemistry, PB 124 Blindern, NO-0314 Oslo, Norway
[b] Department of Chemistry, University of Oslo, Centre for Materials Science and Nanotechnology, FERMiO, Gaustadalleen 21, NO-0349 Oslo, Norway
[c] Norwegian University of Science and Technology (NTNU), Department of Materials Science and Engineering, NO-7491 Trondheim, Norway

ARTICLE INFO

ABSTRACT

For breakthrough development in solid oxide fuel cells, novel cell architectures integrating better performing materials and cost-effective manufacturing processes with potential for mass production must be realised. The present work addresses this on the basis of the recent discovery of acceptor doped rare-earth ortho-niobate proton conductors and the development of a versatile fabrication process. La$_{0.995}$Sr$_{0.005}$NbO$_{4-\delta}$/NiO anodes are produced by tape-casting and co-lamination of green layers. Their porosity is finely tuned by using a pyrolyzable pore former. La$_{0.995}$Sr$_{0.005}$NbO$_{4-\delta}$ electrolytes are spin-coated using ceramic-based suspensions. Fully dense electrolytes with thickness ranging from 9 μm to 26 μm are obtained after sintering in air at 1350 °C. The cathode layers are then screen-printed. To match thermal expansion and to avoid chemical reaction between the functional layers, special attention is paid to the design of cathode architectures. CaTi$_{0.9}$Fe$_{0.1}$O$_{3-\delta}$, La$_2$NiO$_{4+\delta}$ and La$_4$Ni$_3$O$_{10}$ mixed oxygen ion and electron conducting oxides are investigated as either monophase or La$_{0.995}$Sr$_{0.005}$NbO$_{4-\delta}$-based composite electrodes. The latter gives the whole cell an innovative "semi-monolithic" concept, which can take advantage of the chemical and mechanical stability of La$_{0.995}$Sr$_{0.005}$NbO$_{4-\delta}$, as well as of inherent material integration. Most promising cell architectures are finally selected based on thermo-mechanical and chemical compatibility of all functional layers.

© 2008 Elsevier B.V. All rights reserved.

1. Introduction

High temperature proton conductors have recently received an increasing attention as alternative electrolyte materials for solid oxide fuel cells. In comparison to their oxygen ion conducting counterparts (SOFC), proton conducting fuel cells (PCFCs) would offer higher intrinsic thermodynamic efficiency with hydrogen-rich fuels [1,2] and simpler balance of plant (BOP). In PCFCs, water vapour is produced at the cathode rather than at the anode, thereby preventing fuel dilution. High conversion efficiency may thus be reached [3]. Nevertheless, the current status of PCFCs falls well beyond expectation. This mainly stems from the lack of proton conductors meeting materials requirements for long-term operation: proton conductivity in the order of 10^{-2} S cm^{-1} at the operating temperature, none or low electronic conductivity and long-term

stability [4–7]. These demands strongly reduce the number of potential electrolyte materials. Currently, most extensively studied proton conducting electrolytes are based on perovskite-type materials [8]. These, however, face a general "trade-off" limitation between permeability and stability. This is especially relevant when operating the cells at middle to high pressure of CO$_2$ and/or H$_2$O [9,10]. In the search for new materials, acceptor substituted rare-earth ortho-niobates and ortho-tantalates Ln(Nb/Ta)O$_4$ oxides were recently demonstrated to exhibit appreciable proton conductivity in wet atmospheres [11]. The maximum proton conductivity reported so far confines to ~10^{-3} S cm^{-1} for 1% Ca-doped LaNbO$_4$ [11,12]. Despite a proton conductivity one order of magnitude lower than the targeted value, the long-term chemical stability and the relatively low grain boundary impedance reported for this class of materials make them of potential interest for application in PCFCs.

Another key hurdle for efficient PCFC development lies on suitable cell design and especially, advanced electrode architectures. Ito et al. [13] have probably reported the best performance of PCFCs with a power density of 1.4 W cm^{-2} at 600 °C achieved with a 0.7 μm thick BaCe$_{0.8}$Y$_{0.2}$O$_{2.90}$ electrolyte integrated in a Pd-

* Corresponding author. Tel.: +33 4 67 14 91 58; fax: +33 4 67 14 91 19.
E-mail addresses: Marie-Laure.Fontaine@iemm.univ-montp2.fr, Marie-Laure.Fontaine@sintef.no (M.-L. Fontaine).

supported cell. Higher cell efficiency may be reached with further decrease in the electrolyte thickness, though the mechanical stability of such thin electrolyte would be questionable. Moreover, as the IR-loss across the electrolyte decreases, electrode resistance is likely to become predominant and limit the overall cell efficiency. High voltage losses across metallic or monophase ceramic cathodes have already been reported in thin electrolyte-based cells [14–18]. Graded or composite electrodes would therefore be of promising interest to reduce the polarisation resistance in these cells [19,20].

These reports pinpoint the need for selecting suitable materials and purposeful design strategy to match thermal, mechanical and chemical compatibility of all functional layers in a single cell. Accordingly, the present paper deals with the development of innovative PCFCs integrating strontium doped lanthanum ortho-niobate $La_{0.995}Sr_{0.005}NbO_{4-\delta}$ (LSNb) as electrolyte material. Three cathode materials were investigated for designing compatible cathode architectures. Firstly, $CaTi_{0.9}Fe_{0.1}O_{3-\delta}$ is a mixed oxide ion, proton and electron conducting perovskite with chemical stability over a large oxygen partial pressure range [21]. This material has a thermal expansion coefficient (TEC) of $10 \times 10^{-6} K^{-1}$, close to that of LSNb of $\sim 8 \times 10^{-6} K^{-1}$. Secondly, $La_2NiO_{4+\delta}$ is the member $n = 1$ of the Ruddlesden-Popper (RP) series $La_{n+1}Ni_nO_{2n+1}$, exhibiting mixed oxide ion and electron hole conduction and showing high oxygen surface exchange coefficient and oxygen diffusion coefficient. The TEC of $La_2NiO_{4+\delta}$ is $14 \times 10^{-6} K^{-1}$. Thirdly, $La_4Ni_3O_{10}$ oxide is the member $n = 3$ of the RP series, and was recently reported with better performance than $La_2NiO_{4+\delta}$ as cathode material in SOFC [22]. This material shows similar thermal expansion as $La_2NiO_{4+\delta}$. Both monophase and composite cathodes were prepared in this work. The single cells were produced by a combination of tape-casting, spin-coating and screen-printing techniques. The structural and microstructural characterization of each material and their assembly are described here. Results were used to identify most promising cell architectures. Electrochemical analyses of the selected cells will be reported in a forthcoming paper.

2. Experimental/materials and methods

2.1. Preparation and characterization of ceramic powders

$La_{0.995}Sr_{0.005}NbO_{4-\delta}$ (LSNb), $CaTi_{0.9}Fe_{0.1}O_{3-\delta}$ (CTF) and $La_2NiO_{4+\delta}$ (L2Ni) powders were synthesized by spray-pyrolysis using water-based solutions according to a method described elsewhere [23]. $La_4Ni_3O_{10}$ (L4Ni3) powder was prepared by a citrate–nitrate method derived from Pechini's work [24]. The powder phase-purity was monitored by X-ray diffraction (XRD) using a Siemens D710 diffractometer and the crystallite size was extracted from the Scherrer formula. The powder morphology was observed by scanning electron microscopy (SEM) with a JEOL JSM-5900LV. The sinterability of LSNb spray-pyrolysed powder was investigated with a dilatometer NETZSCH DIL 402C/4/G. For this purpose, green pellets of 10 mm diameter were heated in air from ambient temperature to 1550 °C, with both heating and cooling rates of 5 °C min^{-1}.

Table 1
Composition of green laminates.

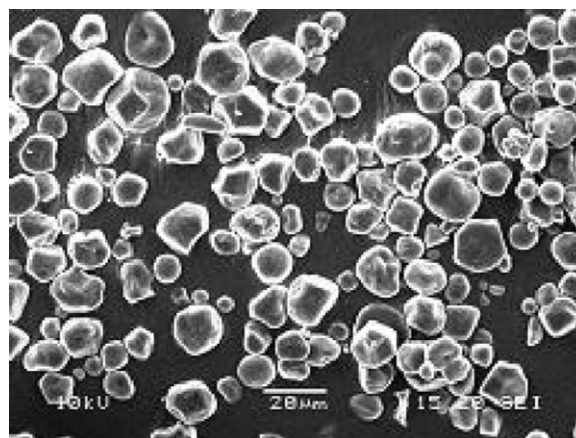| Ceramic powders and additives	Composition (vol.%)
LSNb	14
NiO	14
Corn starch	12
Plasticizers	24
Binder	25
Dispersant	1

Fig. 1. SEM micrograph of corn starch.

2.2. Tape-casting of anodes

LSNb//NiO anode supports were prepared by tape-casting. The preparation of organic-based slurries was based on a two-step process. In the first step, powders of NiO (GFS Chemicals Inc., USA), LSNb, and corn starch filler were dispersed in an organic solution made of a commercial surfactant (KD1, Uniquema, UK) dissolved in an azeotropic mixture of methyl ethyl ketone and ethanol (cf. Table 1). The solutions were milled at 360 rpm for 1 h using a planetary mill with zirconia balls and mortar. During the second step, two plasticizers (polyethylene glycol and dibutyl phtalate) and a commercial binder (polyvinyl butyral B-98, Monsanto, USA) were added in order to confer adequate flexibility and strength to the tapes. The slurries were once more milled for 1 h to achieve good homogeneity. They were cast onto a Mylar^{TM} film and left drying overnight at room temperature in a closed box. Green bodies of 10 cm × 10 cm were obtained by laminating several dried tapes at 45 °C with a pressure of 5 MPa applied for 30 s. Supports with 20 mm diameter were stamped out from the dried green laminates. The thermal decomposition in air of the green laminates was followed up to 1450 °C by thermogravimetric analysis using a SETARAM 92.16.18.

2.3. Spin-coating of electrolytes

Ceramic-based suspensions were prepared by dispersing LSNb powder in a solvent (60 vol.% methylethylketone/40 vol.% terpineol) also containing KD1 dispersant (0.02 wt.%) and B-98 binder (0.03 wt.%). The suspensions were milled for 2 h in a planetary mill.
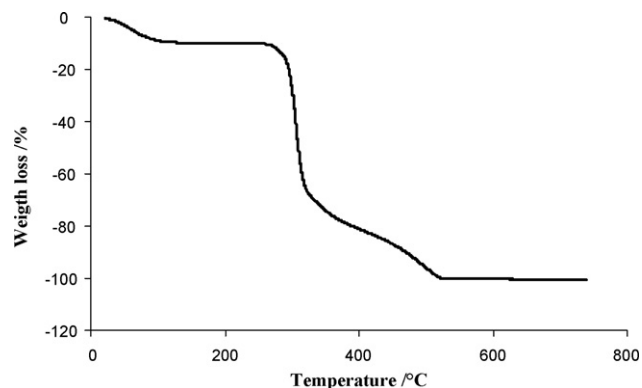

Fig. 2. Thermal decomposition of corn starch filler followed during annealing in air with a heating rate of 100 °C h^{-1}.
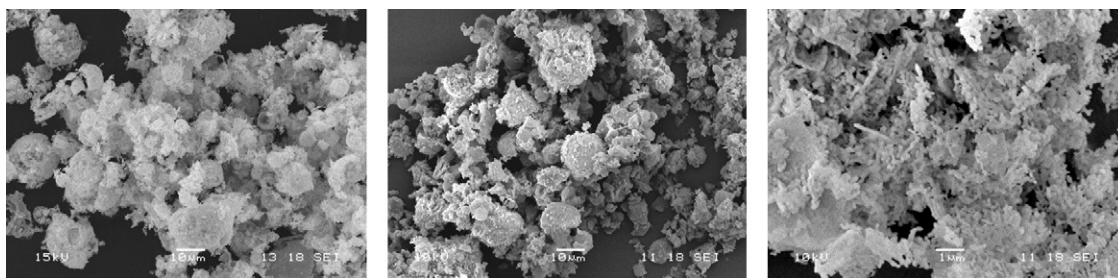
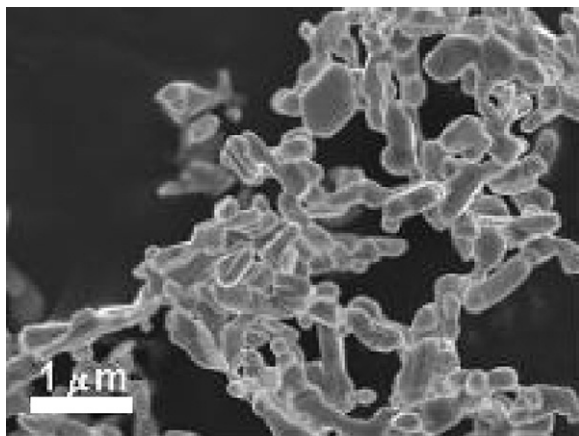**Fig. 3.** SEM micrographs of CTF, L_2Ni and LSNb spray-pyrolysed powders from the left to the right.

Fig. 4. SEM micrograph of L_4Ni_3 powder prepared by Pechini's method.

Fig. 5. Relative contraction (DL/$L0$) of LSNb green pellet upon sintering in the temperature range 20–1500 °C. $L0$ corresponds to the initial thickness of the green pellet, DL = $L - L0$, where L corresponds to the thickness of the pellet upon sintering.

The suspensions were prepared with two ceramic solid loadings of 15 wt.% and 24 wt.%. Each suspension was spin-coated once onto the anodes with a spinning speed of 2000 rpm for 30 s. The resulting half-cells (anodes + electrolytes) were sintered in air using a thermal treatment determined from dilatometry measurements. The sintered samples were annealed in 10% wet H_2 at 900 °C for 3 h to reduce NiO-based anodes.

2.4. Screen-printing of cathodes

Ceramic-based inks were prepared by mixing a commercial organic vehicle (HVS006, Heraeus, GmbH, Hanau) and the ceramic powders (38 wt.%). The cathodes were screen-printed onto non-reduced half-cells with a speed of 40 mm s^{-1}. The resulting single cells (anodes + electrolytes + cathodes) were annealed in air in the temperature range 1100–1300 °C for 2 h with both heating and cooling rates of 100 °C h^{-1}.

2.5. Characterization of bulk materials

Microstructural analyses were performed by SEM coupled to EDS (energy dispersive spectroscopy, Oxford Inca IE 300C with Ge detector). For this purpose, the cells were embedded in an epoxy resin and their cross-sections were carefully polished using SiC grinding papers followed by diamond suspensions down to
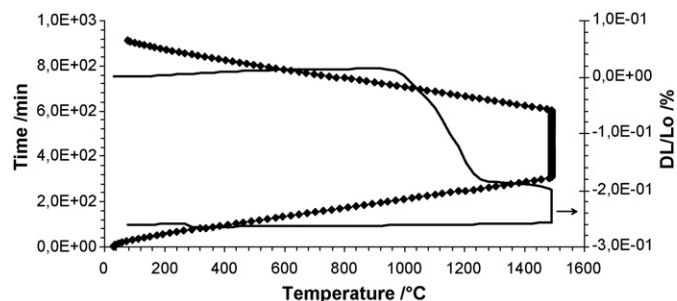
1 μm particle size. SEM images were taken as secondary electron images. Anodes porosity was evaluated by Archimedes method using water. The electrolyte gas tightness and the flow resistance in anodes were examined at ambient temperature using a permeation measurement cell with a rubber gasket sealing. The feed side of the sample was exposed to helium up to maximum 0.6 MPa pressure, while the permeate side was maintained at ambient pressure.

3. Results and discussion

3.1. Characterization of filler and ceramic powders

Corn starch filler has round shaped particles with a mean diameter of about 7 μm (Fig. 1) and is fully decomposed after annealing in air at 600 °C (Fig. 2).

XRD analyses revealed that all ceramic powders were single phase. They consist of agglomerated nano-sized polycrystalline particles with either round (CTF, L_2Ni, LSNb – Fig. 3) or acicular shape (L_4Ni3 – Fig. 4). Powder characteristics given their structure, mean particle size, crystallite size and crystallographic density, are reported in Table 2.

The thermal expansion behaviour of LSNb pellet during annealing in air is depicted in Fig. 5. The pellet starts to shrink around 1010 °C with a maximum contraction of 20% achieved at 1200 °C. The sintering is completed at 1300 °C. After this experiment, a second green pellet was annealed in air at 1350 °C for 2 h. The pellet density reached 99% of the theoretical density in accordance with

Table 2
Characteristics of ceramic powders.

|	LSNb	CTF	L_2Ni	L_4Ni_3
Structure at room temperature	Fergusonite monoclinic	Perovskite cubic	Ruddlesden-Popper tetragonal	Ruddlesden-Popper tetragonal
Mean particle diameter (±20 nm)	50 nm, 1.5 μm aggregates	150 nm, 2 μm egg-shell aggregates	90 nm, 2 μm egg-shell aggregates	250 nm
Mean crystallite size (±2 nm)	33 nm	25 nm	41 nm	100 nm
Crystallographic density	5.9 g cm^{-3}	4.0 g cm^{-3}	7.0 g cm^{-3}	7.0 g cm^{-3}
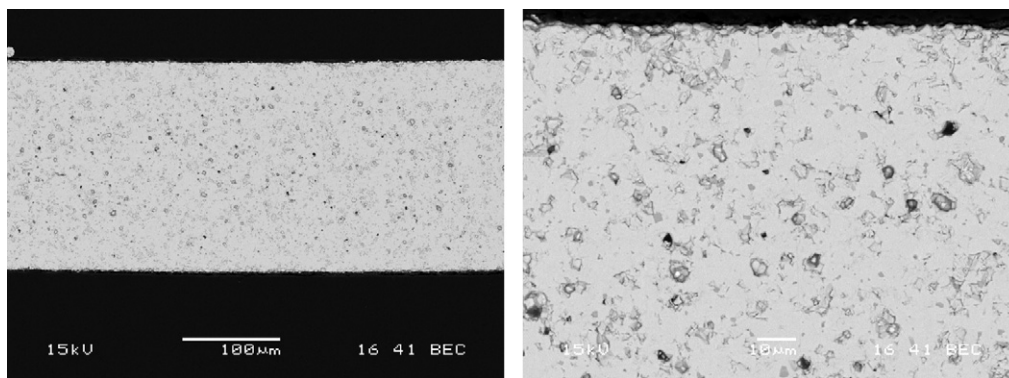
Fig. 6. SEM micrographs with different magnification of LSNb pellet after sintering in air at 1350 °C for 2 h.
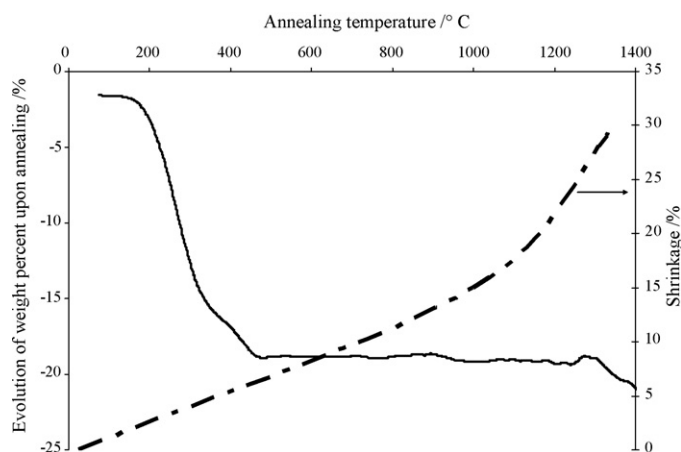

Fig. 7. Weight loss curve and sintering shrinkage of green laminates during annealing in air.

SEM micrograph showing a fully dense sample (Fig. 6). This temperature was thus retained in the following for sintering electrolyte layers.

3.2. Characterization of anodes

The relative weight loss and the concomitant radial shrinkage of tape-cast green laminates during annealing in air are depicted in Fig. 7. A major weight loss of ∼28 wt.% is observed between 200 °C and 500 °C. This value correlates with the amount of organic compounds present in the green laminates of about 30 wt.%. No significant weight loss is further observed up to 1350 °C. This indicates that organic burnout mainly takes place below 500 °C. This weight loss is accompanied with a relative radial shrinkage of ∼4%. The shrinkage increases slowly up to 15% at 1000 °C. A major contraction is further observed in between 1000 °C and 1350 °C with an increase from 15% to 30%, respectively.

LSNb//NiO anodes were annealed at 1000 °C and 1350 °C and their respective SEM micrographs are shown in Fig. 8. Corresponding microstructural parameters are given in Table 3. The anode annealed at 1000 °C (Fig. 8a) exhibits high porosity of about 62% with large macropores of several microns in diameter and small intergranular pores of a few hundred nanometers size. The latter indicates poor sintering of the ceramics, in agreement with dilatometry results and low shrinkage of the sample at this temperature. Increasing the annealing temperature up to 1350 °C causes significant grain growth and removal of the intergranular porosity (Fig. 8b). The remaining macropores are homogeneously distributed throughout the composite matrix and their shape and size are consistent with those of the corn starch grains. Further, the open porosity is about 12 vol.%, which is in good agreement with the volume of corn starch initially present in the dried green laminate (cf. Table 1). It is therefore concluded that the large macropores present in the sintered anode mainly result from the thermal decomposition of the pyrolyzable filler. This is in line with previous work reported for this type of pore former [25,26]. The macropores are well connected, as demonstrated by the high He permeance measured for these samples at room temperature (Fig. 9).
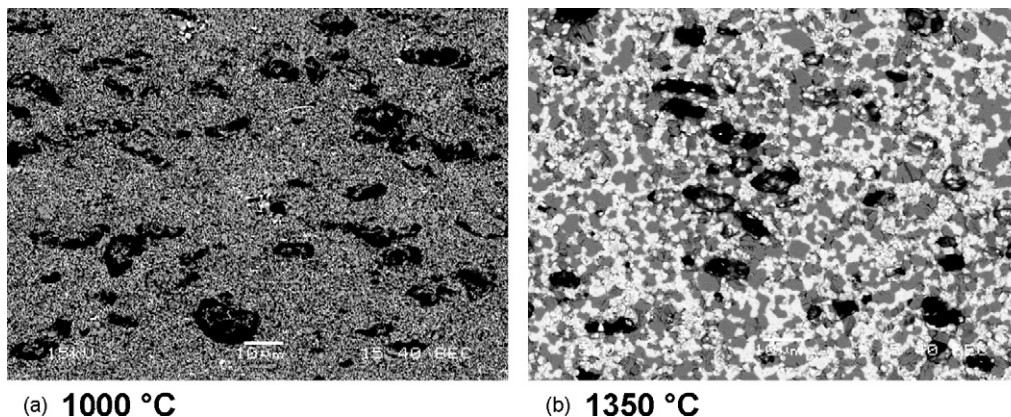

(a) **1000 °C**   (b) **1350 °C**

Fig. 8. SEM micrographs of LSNb//NiO anodes annealed at various temperatures.

Table 3
Anode microstructural parameters.

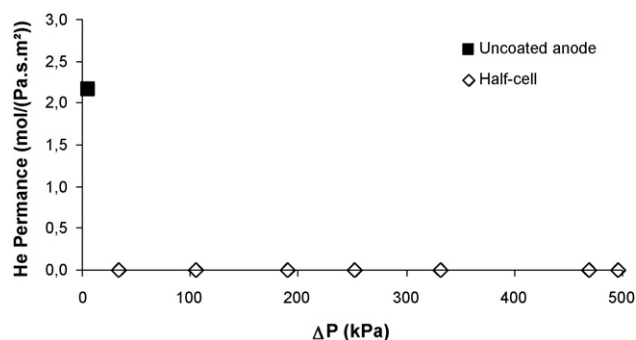|	Green body	LSNb//NiO 1000 °C	LSNb//NiO 1350 °C
Average volume of pore former ($\pm2\%$)	13	×	×
Average pore size ($\pm0.2\,\mu m$)	×	100–500 nm, 10–15 μm	4.0–7.0 μm
Average porosity ($\pm3\%$)	×	62	12
Average grain size ($\pm0.2\,\mu m$)	×	NiO: 200 nm, LSNb: 150 nm	NiO: 1 μm, LSNb: 500–700 nm

Fig. 9. He permeance at room temperature for uncoated anodes and half-cells sintered at 1350 °C.

Fig. 11. SEM micrographs of LSNb/Ni supported cells after reduction in 10% wet H_2.

3.3. Characterization of half-cells

Attempts were made to spin-coat the electrolyte layer onto the green anode followed by co-sintering of the green assembly. Bended half-cells with cracked electrolytes were systematically obtained (not shown here). This may be accounted for by swelling of the anode during organic burnout. Other possible reason may deal with shrinka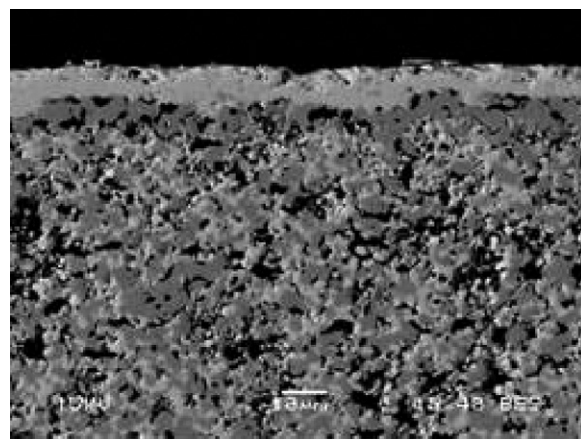ge mismatch during co-sintering because of the large difference in particle packing density in both anode and electrolyte layers. An alternative for the latter issue would be to increase the ceramic solid loading in LSNb suspension. This would however, result in an increased electrolyte thickness, at the detriment of the targeted application.
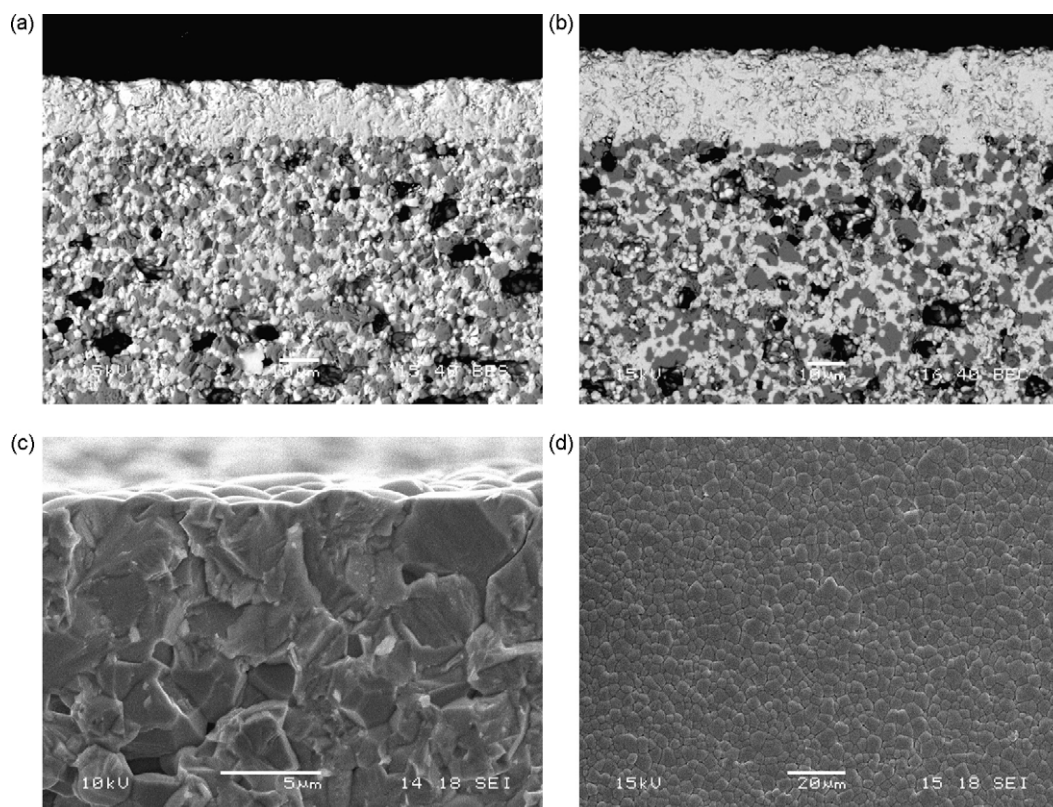

Fig. 10. Backscattered electron micrographs of spin-coated LSNb electrolytes prepared with suspensions containing (a) 15 wt.% of ceramic loading and (b) 24 wt.% of ceramic loading. SEM micrographs of spin-coated electrolyte shown (c) in cross-section view and (d) on surface.
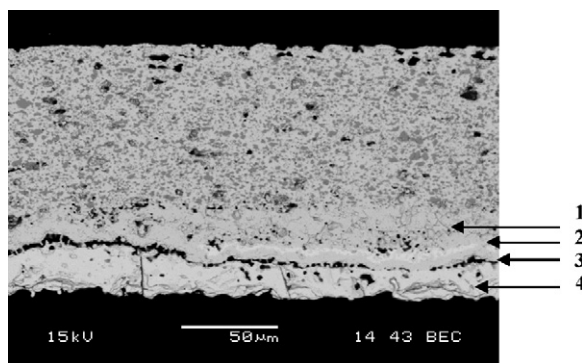
Fig. 12. SEM micrograph of single cell with screen-printed L_2Ni cathode after annealing in air at 1350 °C for 2 h: (1) LSNb electrolyte, (2) and (3) corresponds to secondary phases, and (4) L_2Ni cathode.

Fig. 14. XRD pattern of $LaNb_{1/3}Ni_{2/3}O_3$.

To overcome these problems, the green anodes were pre-annealed at 1000 °C or 1350 °C to monitor the anode shrinkage and to burn organic compounds. Suitable annealing profile was determined from previous results (see Section 3.2). The dried laminates were heating up to 550 °C for 10 h with a slow heating rate of 12 °C h^{-1} for careful control of organic burnout. The temperature was further increased up to 1000 °C or 1350 °C for 2 h. After spin-coating, the half-cells were sintered at 1350 °C for 2 h with both heating and cooling rates of 1.6 °C min^{-1}.

Cross-sections of half-cells prepared with anodes pre-annealed at 1000 °C are shown in Fig. 10a–d. The electrolytes are fully dense and show good adhesion to the underlying anode layers (Fig. 10a and b). No interfacial reaction between the anode and the electrolyte layers is observed. The electrolytes are flat with a thickness increasing from 9 μm to 26 μm with increasing ceramic solid loading in suspensions. Both supported cells underwent a radial shrinkage of ~55% after sintering, as observed earlier for uncoated anodes. This suggests that the half-cell shrinkage is mainly imposed by the anode shrinkage during co-sintering of both electrolyte and
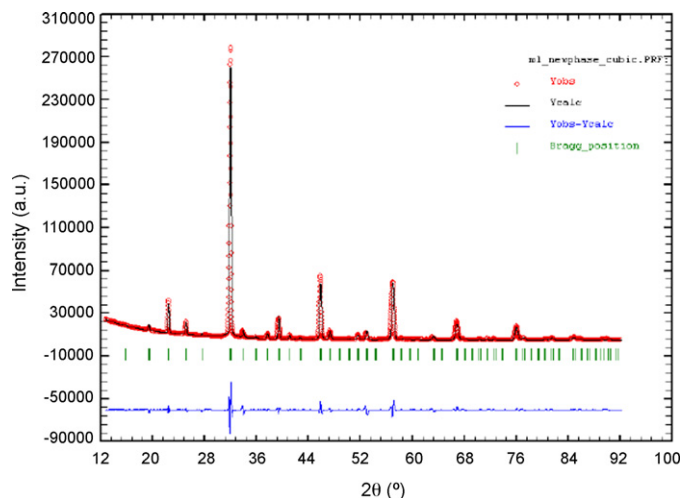
anode layers, as expected from the higher packing density of the thick anodes. No leakage was detected while feeding the half-cell with helium gas up to 6 bars pressure. This indicates that the electrolytes were free of transversal crack or connected pores (Fig. 9 and Fig. 10c and d).

In contrast, the use of anodes pre-annealed at 1350 °C resulted in leaking electrolyte layers. This probably arises from reduced capillary effects due to the removal of small pores in the sintered anodes, yielding inhomogeneous green electrolyte layer with poor adhesion to the underlying support.

The reduction of LSNb//NiO was confirmed by XRD analysis and resulted in an increased porosity up to 37%. The pore size distribution was broadened as smaller pores of about 0.2 μm diameter formed (Fig. 11). The reduced anodes exhibited homogeneous distribution of both pores and metallic nickel.
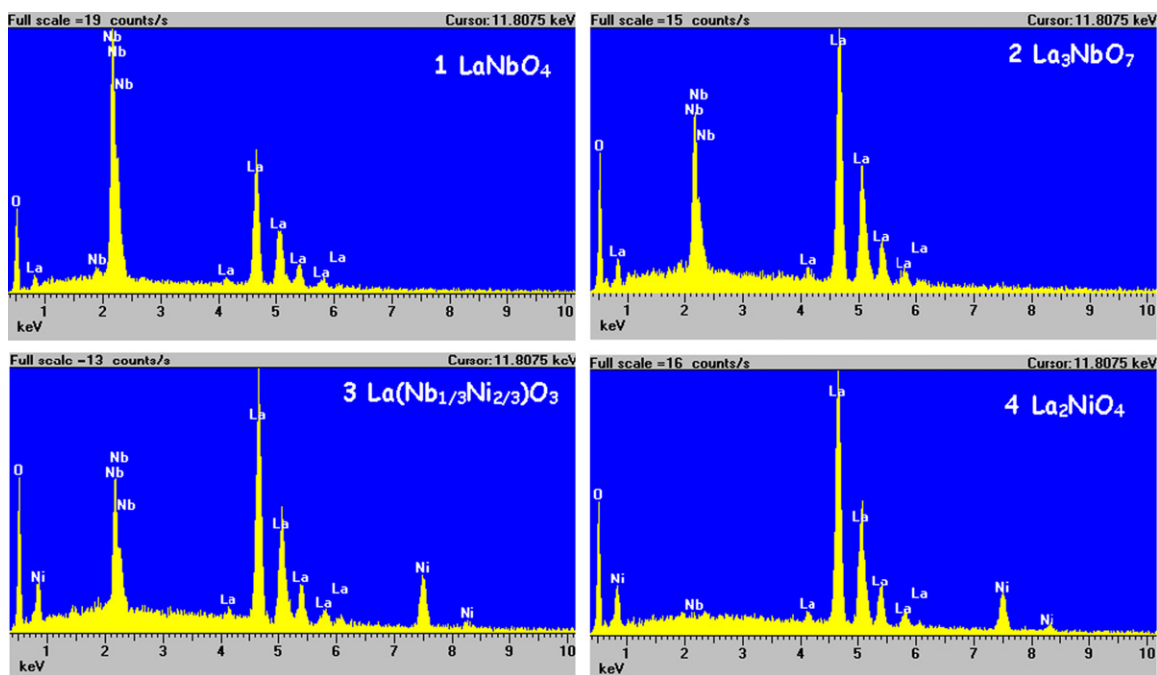

Fig. 13. EDS of single cell with screen-printed L_2Ni cathode after annealing in air at 1350 °C for 2 h: (1) LSNb electrolyte, (2) and (3) correspond to secondary phases, and (4) L_2Ni cathode.
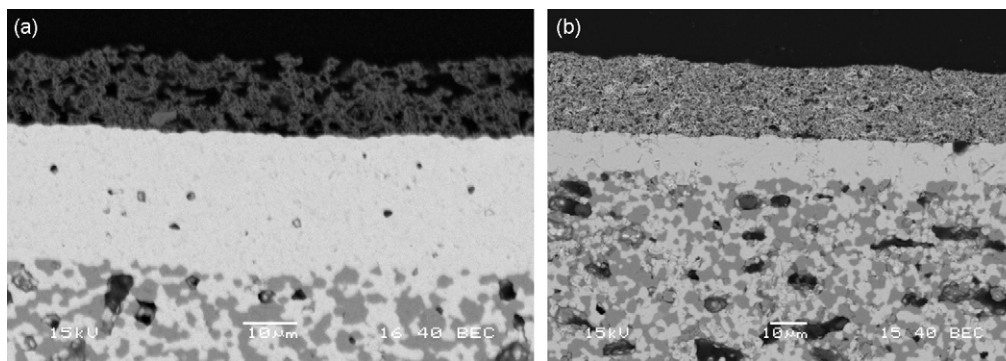
Fig. 15. SEM micrographs of single cells with screen-printed CTF monophase cathode (left) and LSNb//L_4Ni_3 composite cathode (right).

3.4. Characterization of single cells

L_2Ni cathodes were firstly screen-printed onto LSNb electrolyte and annealed up to 1300 °C to promote high adhesion of the electrodes. A cross-sectional view of a single cell is shown in Fig. 12. Two major observations are immediate. A strong delamination has occurred at the cathode/electrolyte interface, which at first glance may be attributed to the difference in TEC of LSNb and L_2Ni (8×10^{-6} K^{-1} versus 14×10^{-6} K^{-1}). This delamination is accompanied with the formation of two secondary phase regions. These phases were identified on the basis of EDS analyses (Fig. 13), XRD pattern (Fig. 14) and Eq. (1), as La_3NbO_7 oxide and a new compound with formula $LaNb_{1/3}Ni_{2/3}O_3$:

$$2LaNbO_4 + 2La_2NiO_4 \rightarrow La_3NbO_7 + 3LaNb_{1/3}Ni_{2/3}O_3 \qquad (1)$$
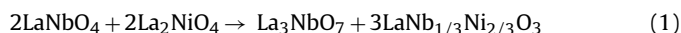
These oxides appeared as a thin layer of about few hundred nanometers thickness on top of the electrolyte, and a thicker layer of about few microns, respectively. The identification of the new $LaNb_{1/3}Ni_{2/3}O_3$ oxide was confirmed from the synthesis of the material in the stoichiometric proportion by means of a protocol similar to the one used for L_4Ni_3 oxide. The material was annealed in air at 1350 °C for 5 h. The resulting black powder was characterized by XRD analysis and preliminary pattern refinement allows for indexing all peaks in a single perovskite phase (Fig. 14). A full structural analysis of this material will be reported in a forthcoming paper [27].

Accordingly, the use of L_2Ni as suitable cathode material for LSNb-based cell is thus very limited. Other alternatives were thus pursued by developing monophase CTF and composite LSNb//L_4Ni_3 cathodes. The former could take advantage of the low TEC of CTF, while the latter could benefit from the composite architecture to match thermal expansion of LSNb and L_4Ni_3. Moreover, the decrease in La/Ni ratio in L_4Ni_3 may hamper diffusion of La^{3+} cation towards the electrolyte, thereby preventing the formation of secondary phases at LSNb//L_4Ni_3 interfaces. Cross-section views of the resulting cells are shown in Fig. 15. As expected, the monophase and composite cathodes were crack-free with a thickness of about 10 μm. Both electrodes showed good bonding to the electrolyte layer and no reaction or delamination at the cathode/electrolyte interfaces was detected. Long-term testing of these cells is now required to assess the stability of these architectures and their power density.

4. Conclusions

In this work, original PCFC devices integrate novel LSNb proton conducting thin film electrolytes with a thickness ranging from 9 μm to 26 μm. The cells were produced by a versatile process combining tape-casting, spin-coating and screen-printing. These reliable techniques make it potentially cost-effective and easy to up-scale. New cathode architectures were investigated by screening several mixed oxygen ion and electron conducting materials. From this preliminary work, it was suggested that L_2Ni may not be chemically compatible with LSNb, whilst CTF monophase cathode and LSNb//L_4Ni_3 composite electrode showed good adhesion and no interfacial reaction with the underlying electrolyte. The fabrication of a composite electrode further enables to design a semi-monolithic cell with LSNb material present in all functional layers. By such, the cell could take advantage of its chemical and mechanical stability and of inherent materials integration. Further, this would contribute to substantial decrease in processing cost of the presently developed fuel cells. Electrochemical testing of these cells is currently in progress and will be discussed in a forthcoming paper.

References

[1] N.Q. Minh, T. Takahashi, Science and Technology of Ceramic Fuel Cells, Elsevier, Amsterdam, 1995.
[2] W.G. Coors, J. Power Sources 118 (2003) 150–156.
[3] P. Ranran, W. Yan, Y. Lisia, M. Zongqiang, Solid State Ionics 177 (2006) 389–393.
[4] T. Norby, R. Haugsrud, R.A. Strøm, T. Grande, K. Wiik, M.-A. Einarsrud, Patent application (2005).
[5] K.D. Kreuer, S. Adams, W. Münch, A. Fuchs, U. Klock, J. Maier, Solid State Ionics 145 (2001) 295–306.
[6] H. Iwahara, Y. Asakura, K. Katahira, M. Tanaka, Solid State Ionics 168 (2004) 299–310.
[7] N. Bonanos, K.S. Knight, B. Ellis, Solid State Ionics 79 (1995) 161–170.
[8] T. Takahashi, H. Iwahara, Rev. Chim. Miner. 17 (1980) 243–253.
[9] K.D. Kreuer, Solid State Ionics 125 (1999) 285–302.
[10] P.I. Dahl, PhD Thesis, NTNU, Trondheim, Norway (2006).
[11] R. Haugsrud, T. Norby, Nat. Mater. 5 (2006) 193–196.
[12] R. Haugsrud, T. Norby, Solid State Ionics 177 (2006) 1129–1135.
[13] N. Ito, M. Iijima, K. Kimura, S. Iguchi, J. Power Sources 152 (2005) 200–203.
[14] W.G. Coors, Proceedings of the 5th European Solid Oxide Fuel Cell Forum, vol. 2, 2002, pp. 602–604.
[15] S. Yamaguchi, T. Shishido, H. Yugami, S. Yamamoto, S. Hara, Solid State Ionics 162–163 (2003) 291–296.
[16] H. Iwahara, Solid State Ionics 77 (1995) 289–298.
[17] T. Schober, Solid State Ionics 162–163 (2003) 277–281.
[18] S. Yamaguchi, S. Yamamoto, T. Shishido, M. Omori, A. Okubo, J. Power Sources 129 (2004) 4–6.
[19] G.C. Mather, F.M. Figueiredo, D.P. Fagg, T. Norby, J.R. Jurado, J.R. Frade, Solid State Ionics 158 (2003) 333–342.
[20] T.L. Ngyuen, K. Kobayashi, T. Honda, Y. Iimura, K. Kato, A. Neghisi, K. Nozaki, F. Tappero, K. Sasaki, H. Shirahama, K. Ota, M. Dokiya, T. Kato, Solid State Ionics 174 (2004) 163–174.

[21] H. Itoh, H. Asano, K. Fukuroi, M. Nagata, H. Iwahara, J. Am. Ceram. Soc. 80 (1997) 1359–1365.
[22] G. Amov, I.J. Davidson, S.J. Skinner, Solid State Ionics 177 (2006) 1205–1210.
[23] T. Mokkelbost, I. Kaus, R. Haugsrud, T. Norby, T. Grande, M.-A. Einarsrud, J. Am. Ceram. Soc. 91 (2008) 879–886.
[24] M.-L. Fontaine, C. Laberty-Robert, A. Barnabé, F. Ansart, P. Tailhades, Ceram. Int. 30 (2004) 2087–2098.
[25] S.F. Corbin, P.S. Apte, J. Am. Ceram. Soc. 82 (7) (1999) 1693–1701.
[26] A. Ianculescu, A. Brăileanu, M. Viviani, L. Mitoşeriu, J. Eur. Ceram. Soc. 27 (2007) 4375–4378.
[27] J. Tolchard, T. Grande, M.L. Fontaine, in preparation.